nature climate change

SUPPLEMENTARY INFORMATION

https://doi.org/10.1038/s41558-019-0603-9

In the format provided by the authors and unedited.

Enhanced equatorial warming causes deep-tropical contraction and subtropical monsoon shift

Wenyu Zhou [1*], Shang-Ping Xie [2] and Da Yang [1,3]

[1]Lawrence Berkeley National Laboratory, Berkeley, CA, USA. [2]University of California, San Diego, La Jolla, CA, USA. [3]University of California, Davis, Davis, CA, USA. *e-mail: wenyuzhou@lbl.gov

Supplementary Information for

"Enhanced equatorial warming causes deep-tropical contraction and subtropical monsoon shift"

Wenyu Zhou[1,*] , Shang-Ping Xie[2] and Da Yang[3,1]

[1]Lawrence Berkeley National Lab, Berkeley, California, USA

[2]University of California, San Diego, La Jolla, California, USA

[3]University of California, Davis, Davis, California, USA

*Corresponding Author: wenyuzhou@lbl.gov

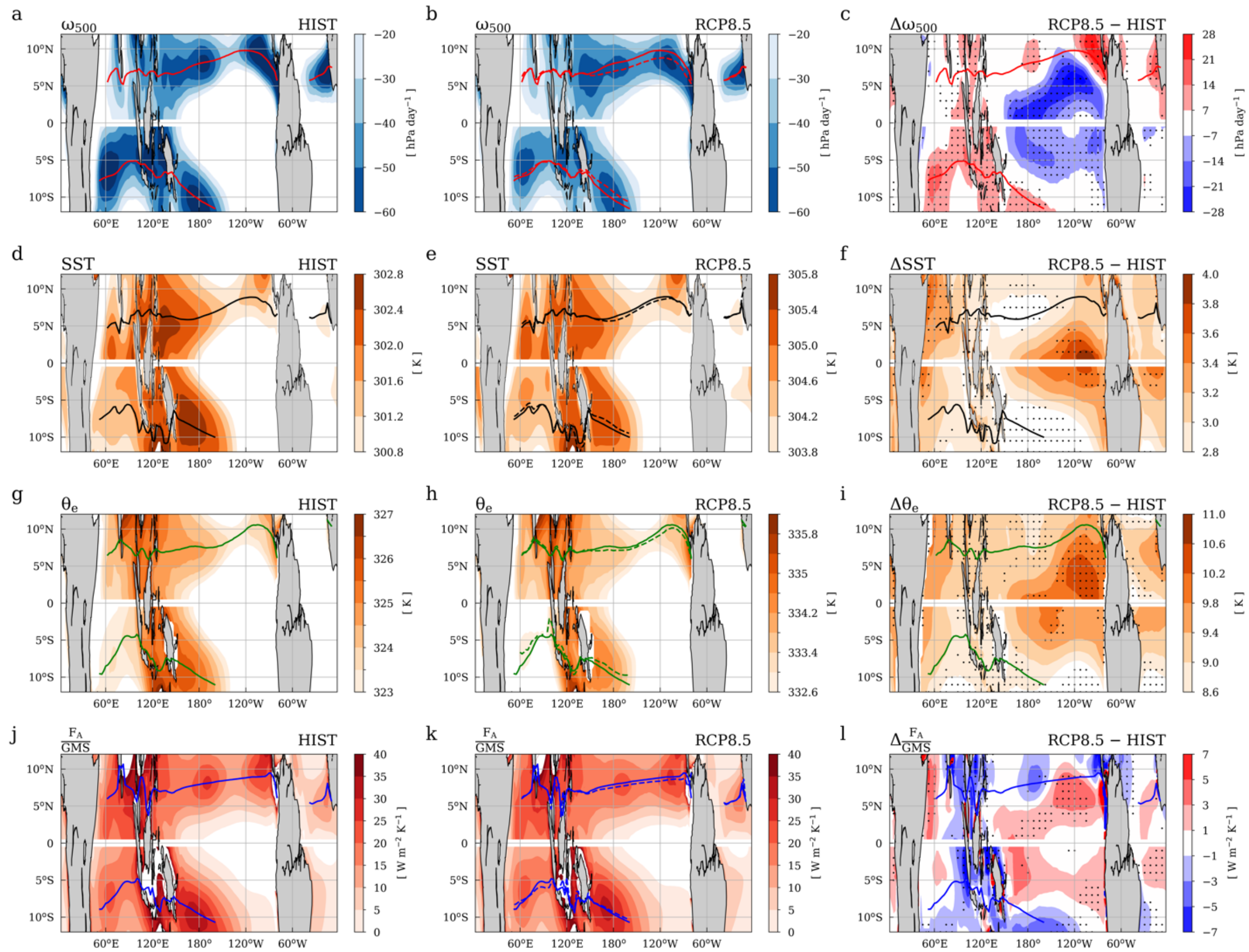

Supplementary Figure 1: ITCZ contraction driven by EEW through coherent thermodynamic and energetic controls. a-c, Summer-mean (Jun-Jul-Aug for NH and Dec-Jan-Feb for SH) pressure vertical velocity at 500hPa (ω_{500}) in HIST (**a**) and RCP8.5 (**b**) and future changes from HIST to RCP8.5 (**c**). The solid and dashed lines show the meridional centroids of the ascending ω_{500} in HIST and RCP8.5, respectively. **d-f**, Same as **a-c** but for the sea surface temperature (SST). **g-i**, Same as **a-c** but for the surface equivalent potential temperature (θ_e). **j-l**, Same as **a-c** but for $\frac{F_A}{GMS}$, the ratio between the energy input into the atmosphere column (F_A) and the gross moist stability (GMS). The meridional centroids of SST and θ_e are computed based on the positive anomaly relative to the 20°S-20°N ocean mean (see Methods for details) while the meridional centroid of $\frac{F_A}{GMS}$ is based on the positive $\frac{F_A}{GMS}$ (negative value masked as 0).

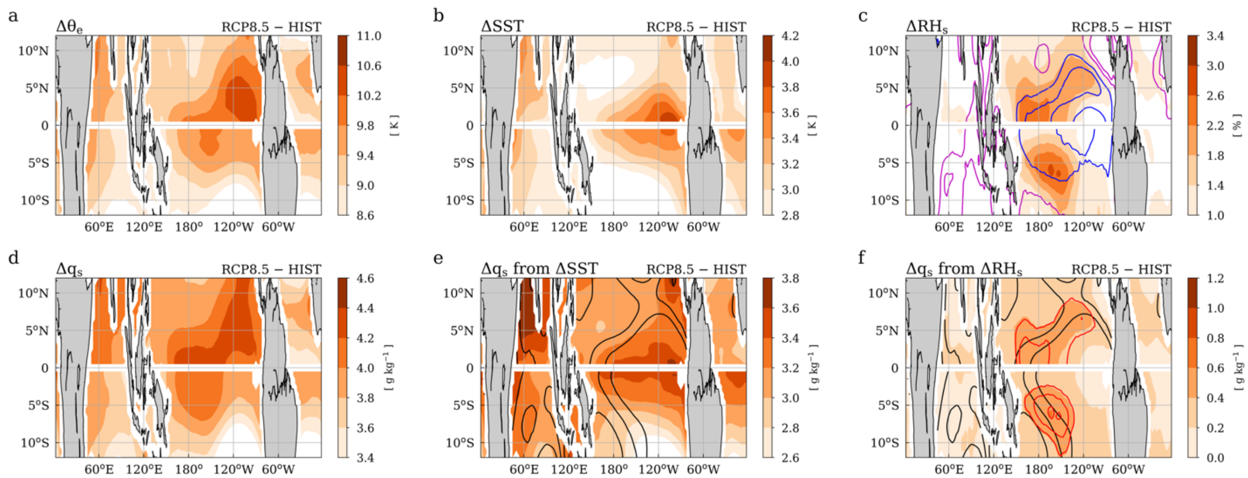

Supplementary Figure 2: Thermodynamic (θ_e) changes driven by EEW and amplified by relative humidity feedbacks associated with the equatorward ITCZ shift. a, Spatial changes in the summer-mean surface equivalent potential temperature (θ_e) under global warming. **b**, Spatial changes in SST. **c**, Spatial changes in surface relative humidity RH_s, which can be understood as a result of the equatorward ITCZ shift. The blue/magenta contours show anomalous ascent/descent associated with the ITCZ shift. **d**, Spatial changes in surface specific humidity q_s. **e**, Spatial changes in q_s contributed from the SST changes (without changes in relative humidity), estimated as $\Delta q_s = RH_s \Delta q_s^* = RH_s \frac{dq_s^*}{dT} \Delta SST = q_s \frac{L_v}{R_v T^2} \Delta SST$. The black contours show the q_s climatology. **f**, Spatial changes in q_s contributed from the relative humidity changes (ΔRH_s), estimated as $\Delta q_s = q_s \frac{\Delta RH_s}{RH_s}$. The black and red contours show q_s climatology and ΔRH_s, respectively. Equatorward shift in θ_e is related to enhanced θ_e in the deep tropics (**a**), which is directly driven by EEW through both the dry (**b**) and moist (**e**) parts, and amplified by the feedback on the moisture (**f**) from the relative humidity changes (**c**) associated with the ITCZ shift itself.

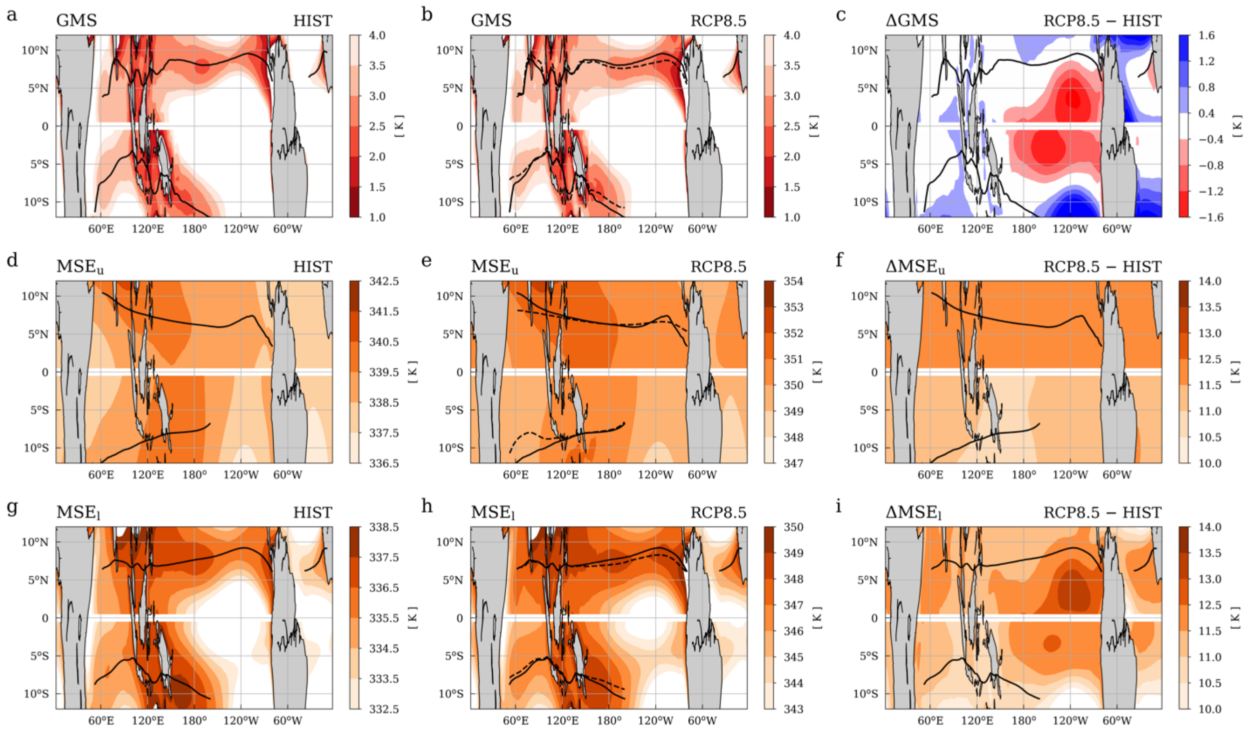

Supplementary Figure 3: Equatorward shift in the gross moist stability (GMS) driven by EEW. a-c, Summer-mean GMS in HIST (**a**) and RCP8.5 (**b**) and future changes from HIST to RCP8.5 (**c**). The solid and dashed lines show the meridional centroids in HIST and RCP8.5, respectively. **d-f**, Same as **a-c** but for the upper-troposphere (150-300hPa) moist static energy (MSE_u). **g-i**, Same as **d-f** but for the lower-troposphere (825-975hPa) moist static energy (MSE_l). Under global warming, MSE_u increases nearly uniformly (**d-f**) due to the weak-temperature-gradient constraint, the equatorward shift in GMS (**a-c**) thus results from the equatorward shift in MSE_l (**g-i**), which is driven by EEW (see Supplementary Fig. 2). The values of MSE and GMS have been normalized by the isobaric specific heat capacity of air.

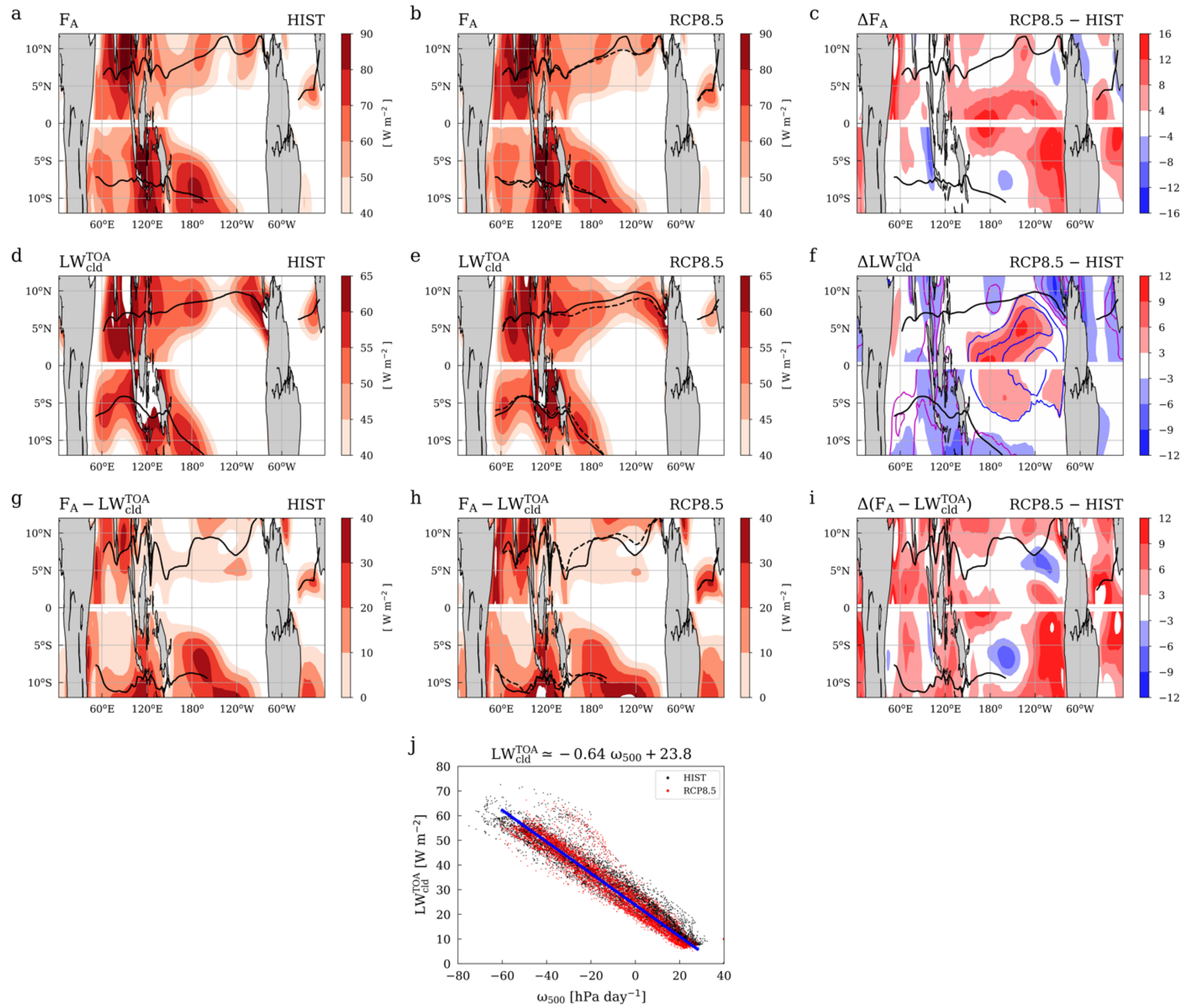

Supplementary Figure 4: ITCZ shift amplified by longwave cloud feedback on the atmospheric energy input (F_A). a-c, Summer-mean F_A in HIST (**a**) and RCP8.5 (**b**) and future changes from HIST to RCP8.5 (**c**). The solid and dashed lines show the meridional centroids in HIST and RCP8.5, respectively. **d-f**, Same as **a-c** but for the longwave cloud radiative effect at the top of the atmosphere (LW_{cld}^{TOA}, downward as positive). **g-i**, Same as **d-f** but for the atmospheric energy input from other sources except LW_{cld}^{TOA}. **j**, LW_{cld}^{TOA} as a linear (and almost invariant) function of the pressure vertical velocity at 500 hPa (ω_{500}) in HIST and RCP8.5 (dots show the seasonal value for grid points over the ocean from 20°S to 20°N; black for HIST and red for RCP8.5). Since LW_{cld}^{TOA} is a linear (and invariant) function of ω_{500}, as the ITCZ shifts equatorward under global warming, LW_{cld}^{TOA} shifts equatorward correspondingly (from **d** to **e**). The spatial changes in LW_{cld}^{TOA} (shading in **f**) closely follow those of ω_{500} (contours in **f**) and thus work as a feedback to amplify the ω_{500} responses to EEW. Other energy sources do not contribute to the equatorward shift in F_A (**g-i**).

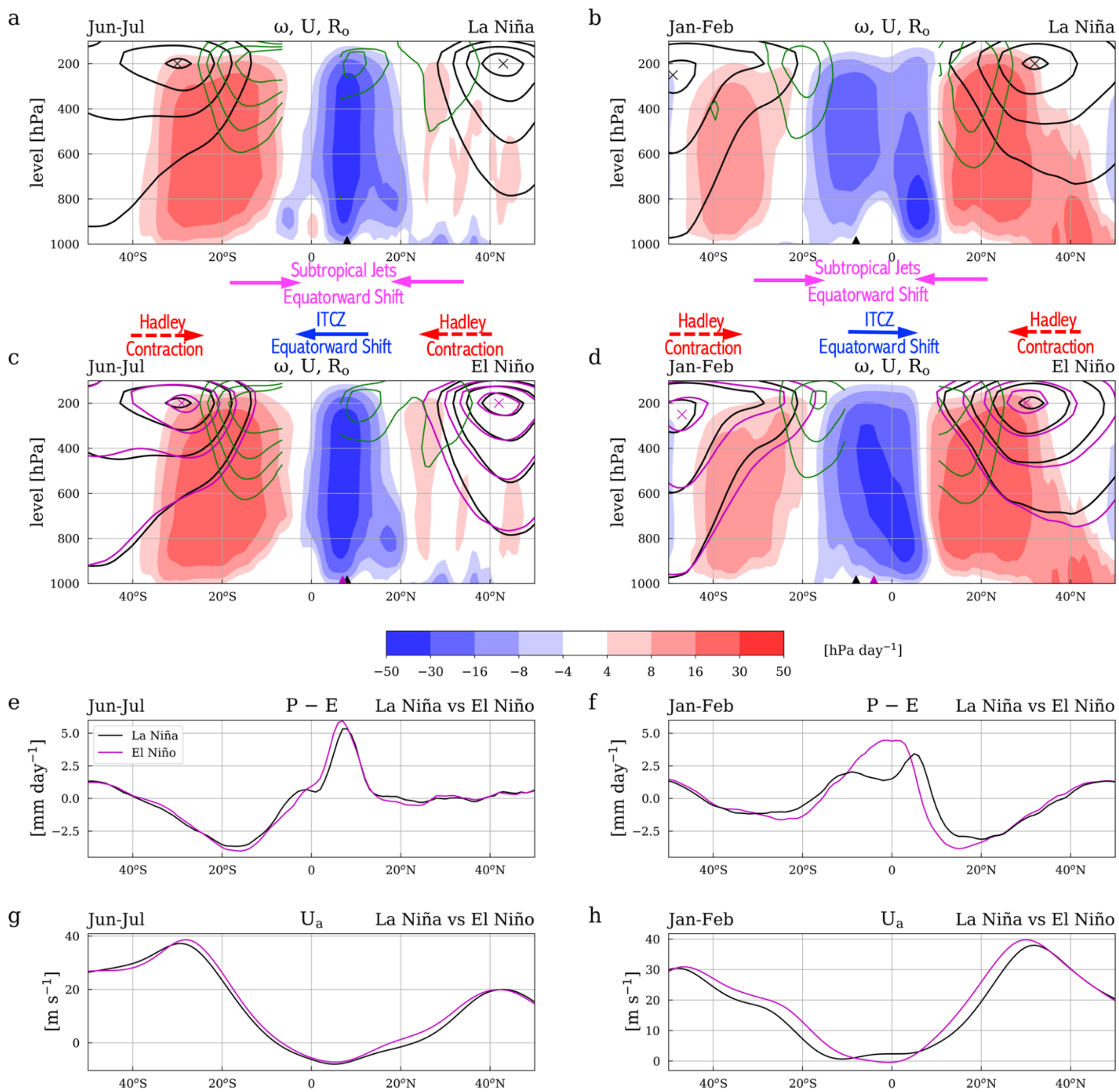

Supplementary Figure 5: Responses of the seasonal zonal-mean circulation to ENSO. **a**,**b**, Zonal-mean pressure vertical velocity (ω, shading), zonal-mean zonal wind (U, black contours) and local Rossby number (Ro, green contours at an interval of 0.1, starting from 0.1 for the summer hemisphere and 0.2 for the winter hemisphere) in Jun-Jul (**a**) and Jan-Feb (**b**) of the La Niña (composite of 1988-1989, 2000-2001, 2011-2012). The local Rossby number is a measurement of how close the zonal wind is to the angular-momentum-conservation and is defined as $\mathrm{Ro} = -\zeta/f$ where $\zeta = -(acos\phi)^{-1}\partial_{\phi}(\mathrm{U}cos\phi)$ is the relative vorticity and a is the Earth radius. **c**,**d**, Same as **a**,**b** but for the El Niño (composite of 1982-1983, 1997-1998, 2015-2016). The zonal wind is shown in contours (black for La Niña and magenta for El Niño). From La Niña to El Niño, the peak ascent at 500 hPa in the deep tropics (denoted by the black triangle for La Niña and the magenta triangle for El Niño) shifts equatorward ("ITCZ equatorward shift"), the poleward edge of the subtropical descent (red shading) shifts equatorward ("Hadley contraction") and the subtropical jet (black contours for La Niña and magenta contours for El Niño) further extends into the tropics ("subtropical jet equatorward shift"). The equatorward shift of the subtropical jet is found to be more pronounced in the summer hemisphere. **e**,**f**, Zonal-mean hydrology imbalance (P - E) in La Niña (black line) and El Niño (magenta line) for Jun-Jul (**e**) and Jan-Feb (**f**), respectively. **g**,**h**, Same as **e**,**f** but for the zonal-mean zonal wind in the upper troposphere (150-300hPa). Note that the ENSO SST signal peaks in winter and is weaker in summer. The ERA-interim reanalysis dataset is used for plotting Supplementary Fig. 5 and 6.

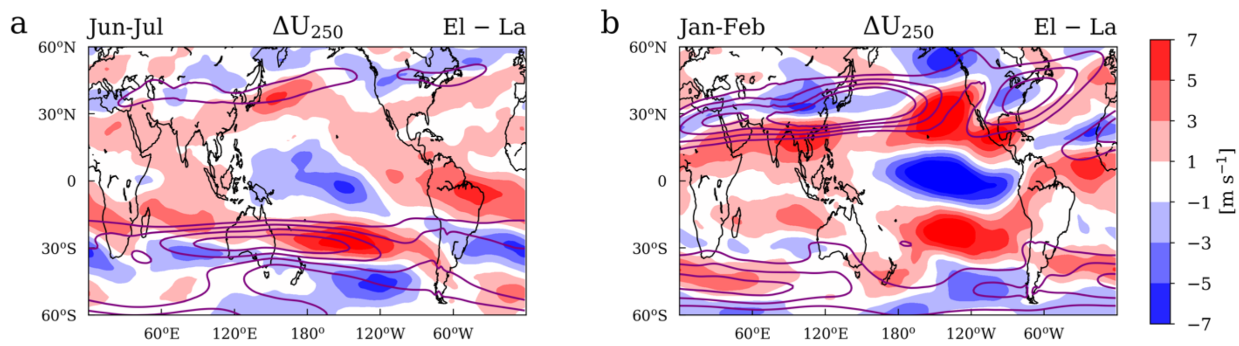

Supplementary Figure 6: Difference in the 250hPa zonal winds between La Niña and El Niño in Jun-Jul (**a**) and Jan-Feb (**b**). The seasonal climatology is shown in purple contours. Equatorward shifts in the subtropical jet are consistently found in both the summer and winter hemispheres in both the developing and peak phases of El Niño.

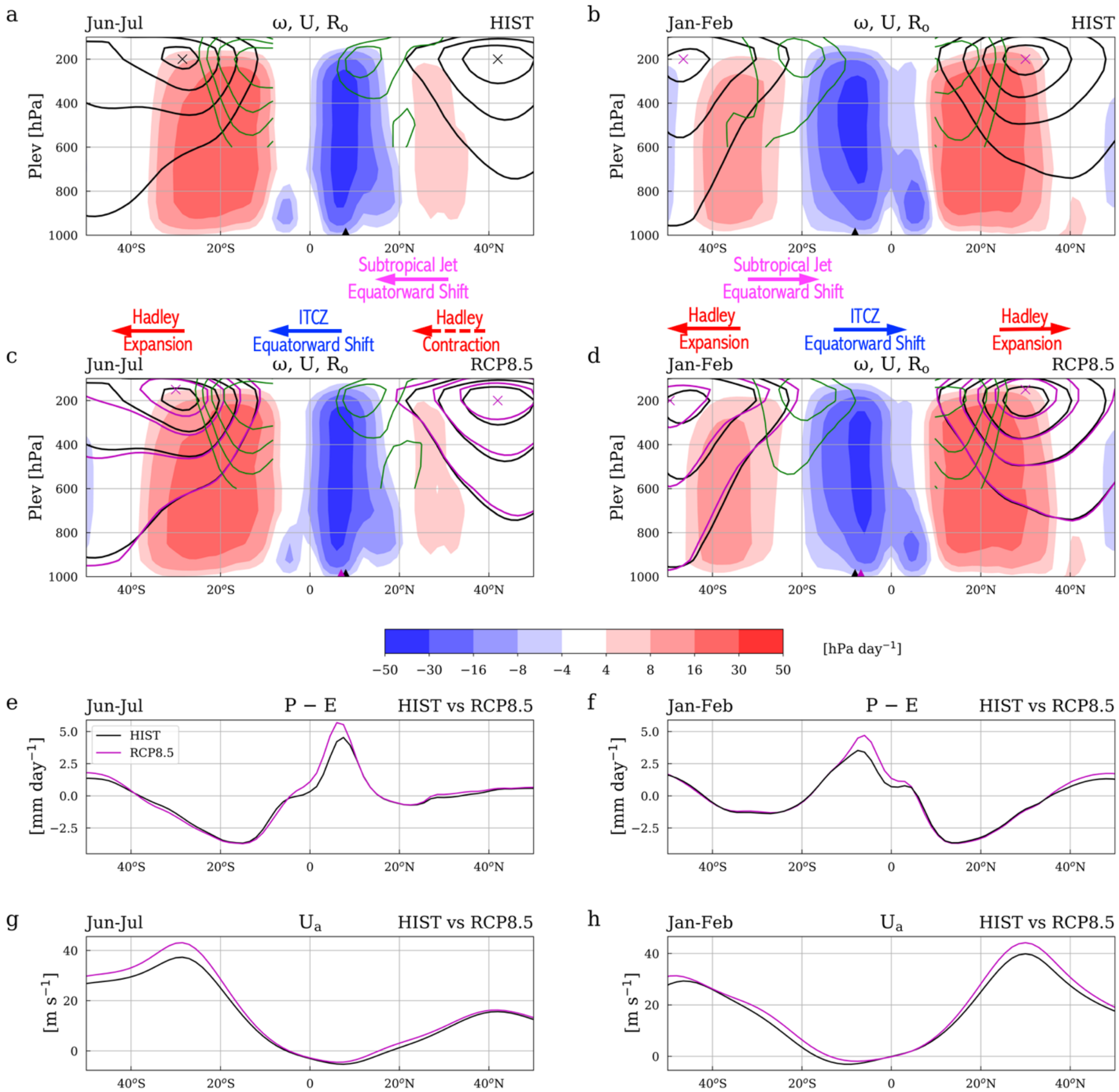

Supplementary Figure 7: Responses of the seasonal zonal-mean circulation to global warming. **a**,**b**, Zonal-mean pressure vertical velocity (ω, shading), zonal-mean zonal wind (U, black contours) and local Rossby number (Ro, green contours at an interval of 0.1, starting from 0.1 for the summer hemisphere and 0.2 for the winter hemisphere) in Jun-Jul (**a**) and Jan-Feb (**b**) for the HIST climatology. **c**,**d**, Same as **a**,**b** but for the RCP8.5 climatology. From HIST to RCP8.5, the ITCZ (denoted by the black triangle for HIST and the magenta triangle for RCP8.5) shifts equatorward. The subtropical jet shifts equatorward in the summer hemisphere (black contours for

HIST and magenta contours for RCP8.5). The Hadley cell, in general, expands poleward but contracts equatorward in the NH early summer (Jun-Jul). **e**,**f**, Zonal-mean hydrology imbalance (P - E) in HIST (black line) and RCP8.5 (magenta line) for Jun-Jul (**e**) and Jan-Feb (**f**), respectively. **g**,**h**, Same as **e,f** but for the zonal-mean zonal wind in the upper troposphere (150-300hPa).

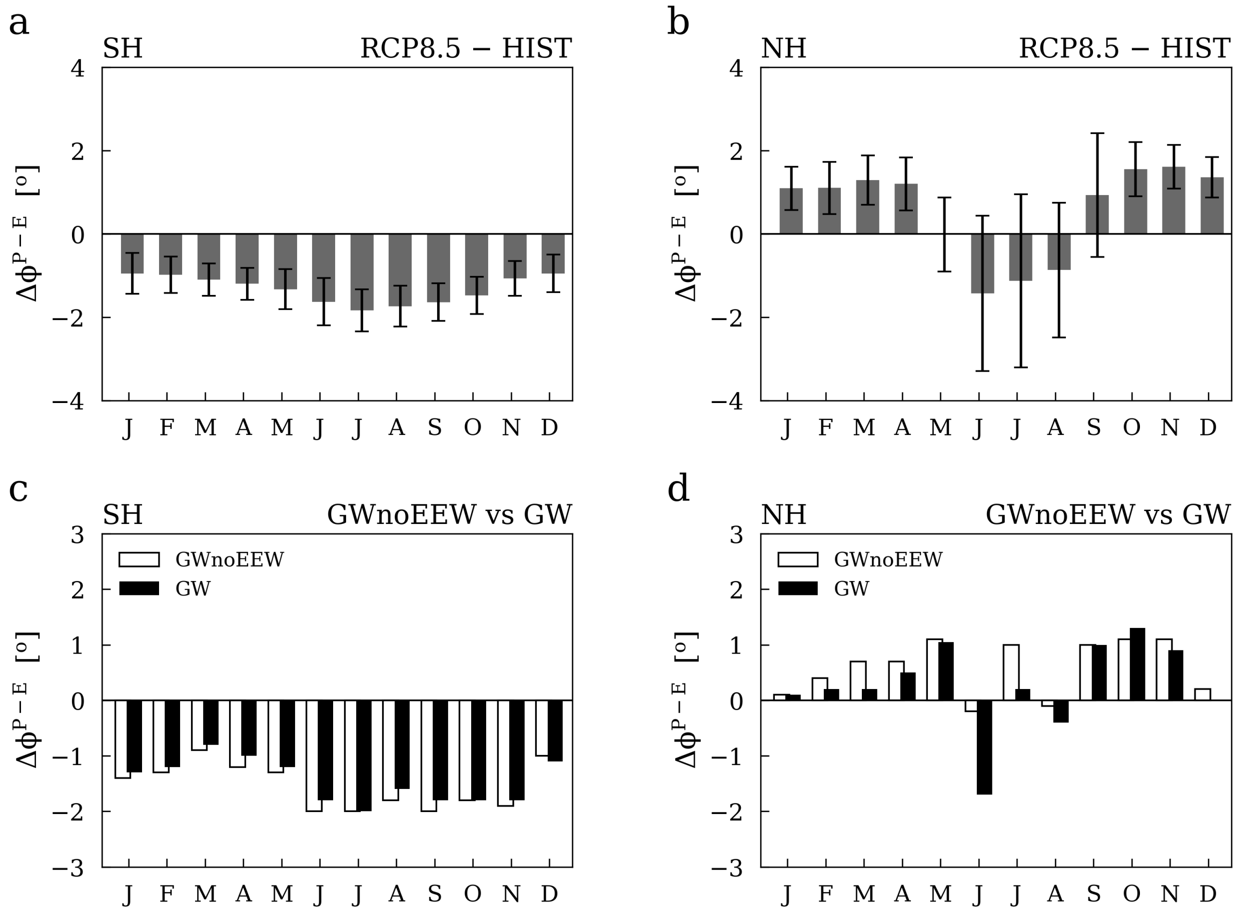

Supplementary Figure 8: Changes in the hydrological boundary. **a**,**b**, Future changes from HIST to RCP8.5 in the zero-crossing latitude of precipitation minus evaporation ($\Delta\phi^{P-E}$) in the SH (**a**) and NH (**b**) for each month. The bars show the ensemble mean and the error bars indicate the multi-model standard deviation in CMIP5 models. **c**,**d**, Same as **a,b** but for the changes in the GFDL-AM2.1 experiment in response to global surface warming without EEW (GWnoEEW, unfilled bars) and to full global surface warming (GW, filled bars) in the SH (**c**) and NH (**d**). The effect of EEW can be seen from the changes from the unfilled to filled bars. There is a notable equatorward shift of the P-E zero-crossing in the NH early summer, consistent with the early-summer Hadley contraction.

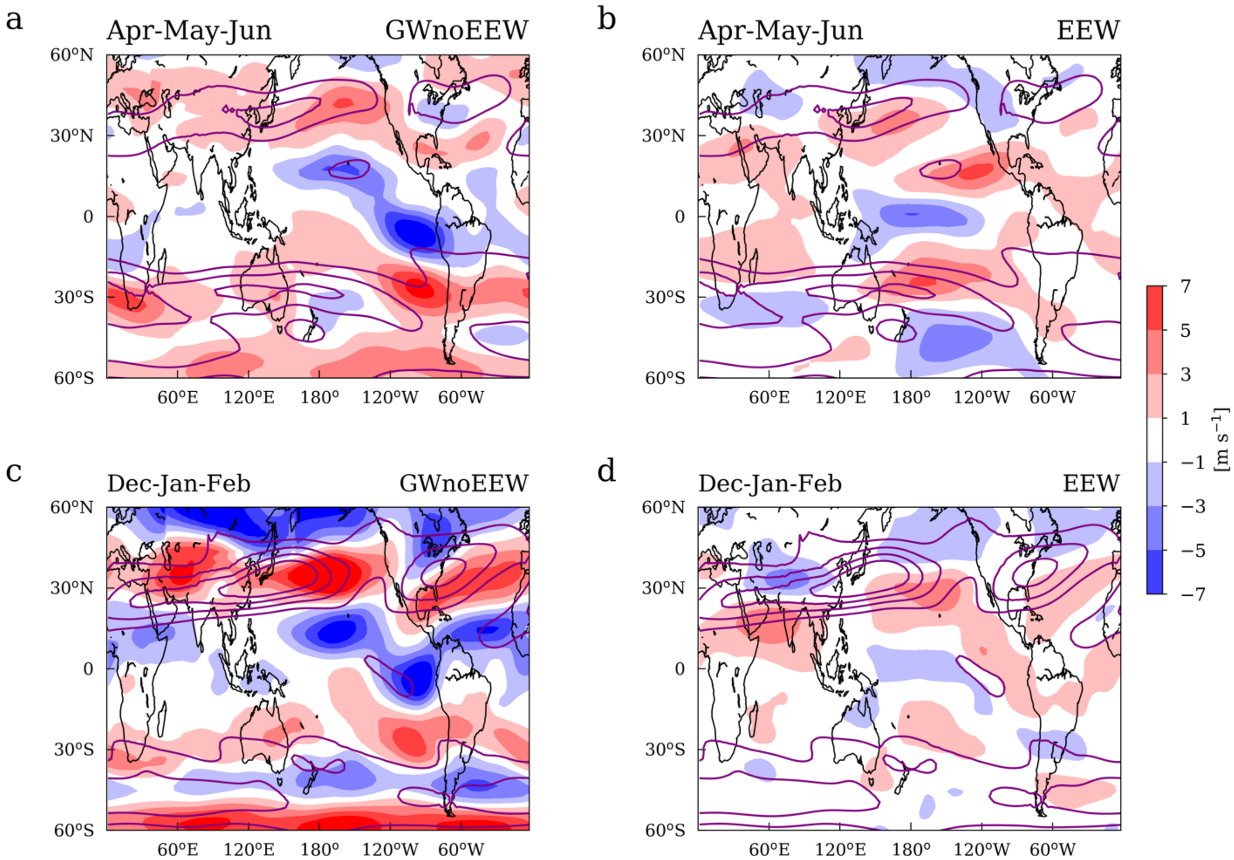

Supplementary Figure 9: Circulation changes in other seasons in the GFDL-AM2.1 experiment. **a**,**b**, Apr-May-Jun changes of the 250hPa zonal winds (U_{250}) in response to GWnoEEW (**a**) and due to EEW (**b**). **c**,**d**, Same as **a**,**b** but for Dec-Jan-Feb. EEW also induces considerable but less dominating equatorward jet shifts in the SH Apr-May-Jun when EEW is strong and in the East Pacific Dec-Jan-Feb when the subtropical jet is rather south. The purple contours show the HIST climatology of the seasonal zonal winds ($\overline{U}_{250}$).

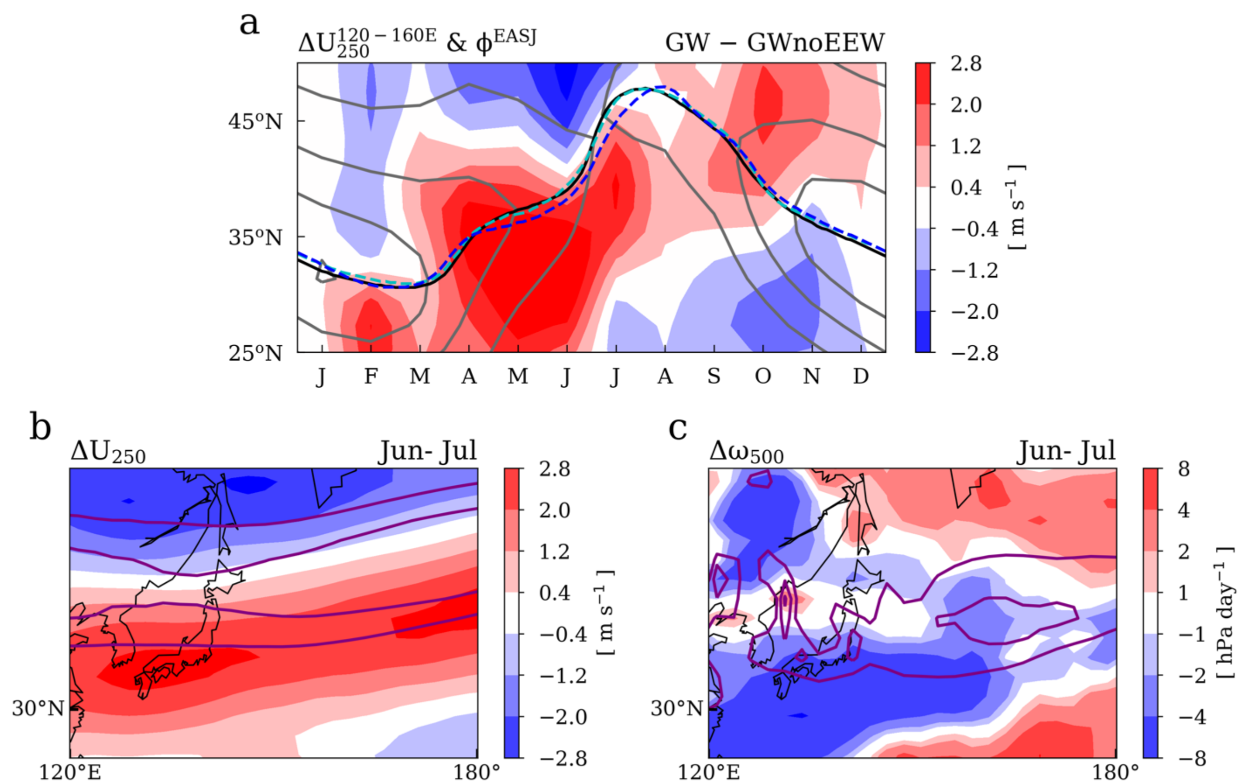

Supplementary Figure 10: Responses of the East Asian summer monsoon to EEW in the GFDL-AM2.1 experiment. **a**, Seasonal changes of the East Asian subtropical jet (EASJ, U_{250} averaged from 120°E to 160°E) due to EEW (from GWnoEEW to GW) in the GFDL-AM2.1 experiment. The monthly climatology is shown in grey contours and the jet core is shown in the solid black line for the control, in the dashed cyan line for GWnoEEW and in the dashed blue line for GW. The jet core shifts equatorward during Jun-Jul only in GW with EEW included. **b**,**c**, Spatial changes of the Jun-Jul U_{250} (**b**) and ω_{500} (**c**) due to EEW in GFDL-AM2.1. The control climatology is shown in purple contours.

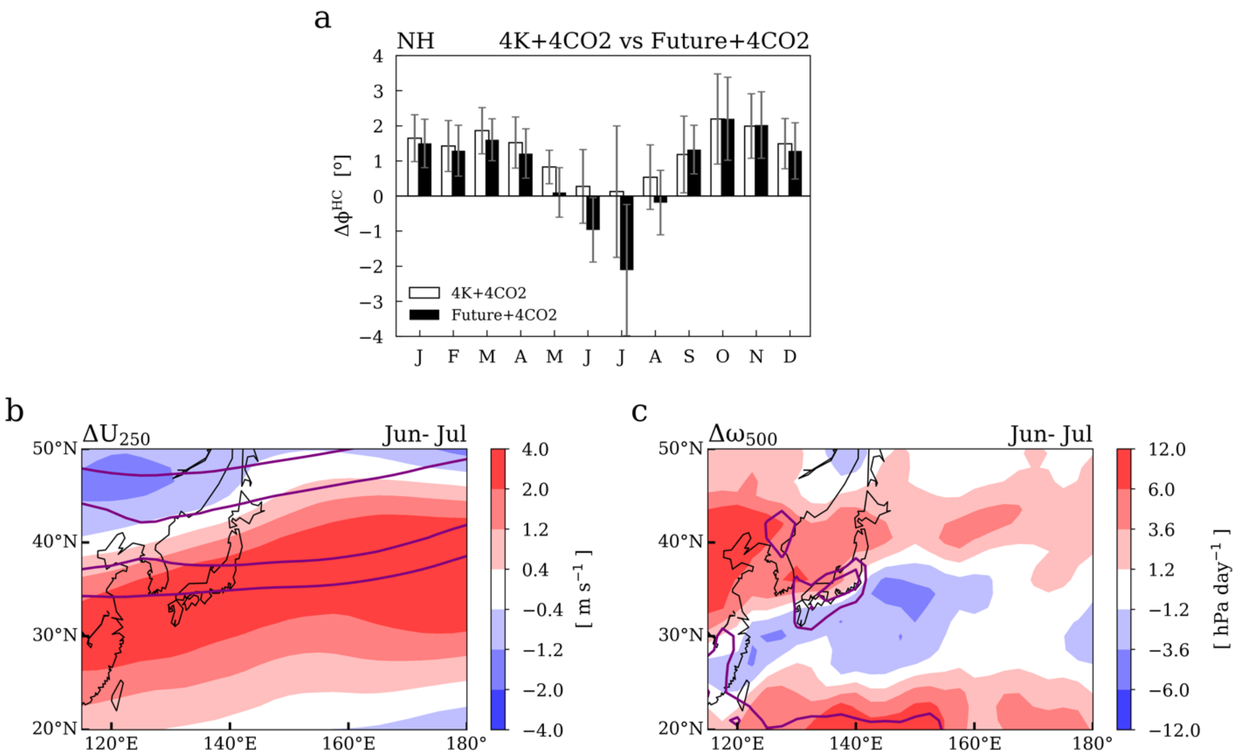

Supplementary Figure 11: NH Hadley cell and EASM changes in response to uniform and patterned warming. a, Future changes in the poleward edge of the NH Hadley cell in response to uniform warming (unfilled bars, AMIP4K) and patterned warming (filled bars, AMIPFuture). The bars show the ensemble mean and the error bars indicate the multi-model standard deviation. The response to direct radiative forcing (which induces a slight poleward expansion in summer), quantified from the AMIP4CO2 experiment, is added to the responses to SST warming so that the plotted changes become more relevant to the coupled RCP8.5 simulations (Fig. 3). **b**,**c**, Spatial changes of the Jun-Jul U_{250} (**b**) and ω_{500} (**c**) from AMIP4K to AMIPFuture.